Title

Diagnostic Ability of Retinal Nerve Fiber Layer Imaging by Swept-Source Optical Coherence Tomography in Glaucoma

Journal

American Journal of Ophthalmology, 159(1)

ISSN

0002-9394

Authors

Yang, Zhiyong
Tatham, Andrew J
Zangwill, Linda M
et al.

Publication Date

2015

DOI

10.1016/j.ajo.2014.10.019

Peer reviewed

Published in final edited form as:
Am J Ophthalmol. 2015 January ; 159(1): 193–201. doi:10.1016/j.ajo.2014.10.019.

Diagnostic ability of retinal nerve fiber layer imaging by swept source optical coherence tomography in glaucoma

Zhiyong Yang[1], **Andrew J. Tatham**[1], **Linda M. Zangwill**[1], **Robert N. Weinreb**[1], **Chunwei Zhang**[1,2], and **Felipe A. Medeiros**[1]

[1]Hamilton Glaucoma Center and Department of Ophthalmology, University of California San Diego, La Jolla, California

[2]Department of Ophthalmology, the First Affiliated Hospital, Harbin Medical University, Harbin, China

Abstract

Purpose—To evaluate the diagnostic accuracies of swept source optical coherence tomography (SS-OCT) wide-angle and peripapillary retinal nerve fiber layer (RNFL) thickness measurements for glaucoma detection.

Design—Cross-sectional case-control study.

Methods—144 glaucomatous eyes of 106 subjects and 66 eyes of 42 healthy subjects from the Diagnostic Innovations in Glaucoma Study were enrolled in this study. Glaucoma was defined by the presence of repeatable abnormal standard automated perimetry results and/or progressive glaucomatous optic disc change on masked grading of stereophotographs. Wide-angle and peripapillary RNFL thicknesses were assessed using SS-OCT. Peripapillary RNFL thickness was also evaluated using spectral-domain OCT (SD-OCT). Areas under the receiver operating characteristic (ROC) curves were calculated to evaluate the ability of the different SS-OCT and SD-OCT parameters to discriminate glaucomatous from healthy eyes.

Results—Mean (± standard deviation) average SS-OCT wide-angle RNFL thickness were 50.5 ± 5.8 μm and 35.0 ± 9.6 μm in healthy and glaucomatous eyes, respectively ($P < 0.001$).

Corresponding Author: Felipe A. Medeiros, M.D., Ph.D., Hamilton Glaucoma Center, University of California San Diego, 9500 Gilman Drive, La Jolla, CA 92093-0946, Telephone: 858-822-4592, Fax: 858-822-0615, fmedeiros@ucsd.edu.

DISCLOSURE

Financial Disclosure(s):
Drs. Zangwill, Weinreb, and Medeiros receive research support from Carl-Zeiss Meditec (Dublin, California); Heidelberg Engineering (Heidelberg, Germany); and Topcon (Tokyo, Japan). Dr. Weinreb receives resource support from Optovue (Fremont, California). Drs. Medeiros and Weinreb are consultants to Carl-Zeiss Meditec. Dr. Weinreb is a consultant to Topcon, Inc. Dr. Medeiros has received research support from Topcon, Inc.. Drs. Yang, Tatham, and Zhang have no financial disclosures.

Authors' contributions:
Involved in Design and conduct of study (Drs Yang, Tatham, Zhang, Weinreb, Zangwill and Medeiros); Collection, management, analysis, and interpretation of data (Drs Yang, Tatham, Zhang, Weinreb, Zangwill, and Medeiros); and preparation, review, or approval of manuscript (Drs Yang, Tatham, Zhang, Weinreb, Zangwill, and Medeiros).

Corresponding values for SS-OCT peripapillary RNFL thickness were 103.5 ± 12.3 μm and 72.9 ± 16.5 μm, respectively (P < 0.001). Areas under the ROC curves of SS-OCT wide-angle and peripapillary RNFL thickness were 0.88 and 0.89, respectively. SS-OCT performed similarly to average peripapillary RNFL thickness obtained with SDOCT (area under the ROC curve of 0.90).

Conclusion—SS-OCT wide-angle and peripapillary RNFL thickness measurements performed well for detecting glaucomatous damage. Diagnostic accuracies of the SS-OCT and SD-OCT RNFL imaging protocols evaluated in this study were similar.

INTRODUCTION

Glaucoma is characterized by progressive loss of retinal ganglion cells with associated structural changes at the level of the optic nerve head (ONH) and retinal nerve fiber layer (RNFL). Considerable evidence has accumulated with regard to the role of structural measurements for diagnosing glaucoma and detecting progression. Structural changes in the ONH and RNFL often are visible before the appearance of detectable loss with standard functional testing.[1–4] Therefore, technologies that can objectively evaluate these structures have become important tools for early diagnosis and follow-up of the disease.

Optical coherence tomography (OCT) provides objective and reliable structural evaluation of the ONH, RNFL and macula. Compared with earlier time domain OCT, spectral domain OCT (SD-OCT) has improved the ability to detect and monitor glaucoma.[5–7] More recently, a new generation of OCT, swept source OCT (SS-OCT) has been introduced.[8] These devices use a short cavity swept laser with a tunable wavelength of operation, instead of the superluminescent diode laser used in SD-OCT. Deep Range Imaging OCT (DRI-OCT-1 Atlantis, Topcon, Tokyo, Japan) is a recently introduced SS-OCT with a center wavelength of 1,050 nm and a sweeping range of approximately 100 nm, compared to the fixed 850 nm wavelength typical of SD-OCT.[9, 10] The instrument also uses two parallel photodetectors to achieve a scan rate of 100,000 A-scans per seconds compared to the 40,000 A-scans per second scanning rate that is typical of SD-OCT devices.

Early studies have demonstrated the ability of SS-OCT to image deep ocular structures such as the choroid and lamina cribrosa, as well as the RNFL thickness.[9, 11–13] In addition, the faster scan speed of SS-OCT facilitates acquisition of a high quality wide-angle scan image containing a large area of the posterior pole, including both the optic disc and macula.

The aim of the present study was to evaluate the ability of average and sectoral RNFL thickness measurements obtained using the SS-OCT wide-angle and optic disc scans to differentiate glaucomatous from healthy eyes. Diagnostic ability was compared to that of peripapillary RNFL measurements obtained using SD-OCT in the same eyes.

METHODS

This was a cross-sectional observational study of participants from the Diagnostic Innovations in Glaucoma Study (clinicaltrial.gov identifier: NCT00221897, National Eye Institute) at the University of California San Diego (UCSD). Diagnostic Innovations in Glaucoma Study is a prospective longitudinal study designed to evaluate optic nerve

structure and visual function in glaucoma. Informed consent was obtained from all participants, and the institutional review board (IRB # 140276) and human subjects committee at UCSD approved all methods. All study methods adhered to the tenets of the Declaration of Helsinki for research involving human subjects and the study was conducted in accordance with the regulations of the Health Insurance Portability and Accountability Act.

Methodological details of the Diagnostic Innovations in Glaucoma Study have been described in detail previously.[14] In brief, at each visit during follow-up, subjects underwent a comprehensive ophthalmologic examination including review of medical history, best-corrected visual acuity, slit-lamp biomicroscopy, intraocular pressure (IOP) measurement, gonioscopy, dilated fundoscopic examination, stereoscopic optic disc photography, and standard automated perimetry (SAP) using the Humphrey Field Analyzer II (Carl Zeiss Meditec, Dublin, CA, USA) and the Swedish Interactive Threshold Algorithm (SITA Standard 24-2). The study included only subjects with open angles on gonioscopy. Subjects were excluded if they presented with a best-corrected visual acuity less than 20/40, spherical refraction outside ± 5.0 diopters or cylinder correction outside 3.0 diopters, or any other ocular or systemic disease that could affect the optic nerve or visual field.

All SAPs were evaluated by the UCSD Visual Field Assessment Center.[15] Visual fields with more than 33% fixation losses or false-negative errors, or more than 15% false-positive errors, were excluded, with the exception of visual fields that had more than 33% false-negative errors in advanced disease. SAP tests were defined as normal if the mean deviation (MD) and pattern standard deviation (PSD) were within 95% normal confidence limits and the Glaucoma Hemifield Test (GHT) was also within normal limits. An abnormal SAP test was defined as a visual field with a PSD with $P < 0.05$ and/or a GHT outside normal limits. Digitized film and digital stereoscopic images were acquired by stereoscopic optic disc photography (Kowa Nonmyd WX3D, software version VK27E, Kowa Company Ltd, Tokyo Japan), and were reviewed for progressive changes by two or more experienced graders who were masked to the subject's identity and to other test results at the UCSD Optic Disc Reading Center.[15–17]

Eyes were classified as glaucomatous if they had repeatable (≥2 consecutive) abnormal SAP test results. Eyes were also classified as glaucomatous if they had documented evidence of progressive optic disc changes on masked grading of stereophotographs, with or without an abnormal SAP result. Healthy subjects were recruited from the general population through advertisements or from the staff and employees at the University of California, San Diego. Healthy subjects had IOP less than 22 mmHg with no history of increased IOP and normal SAP in both eyes.

Optical Coherence Tomography

RNFL thickness was assessed from images acquired using the swept source Deep Range Imaging-OCT (DRI-OCT-1, Topcon, Tokyo, Japan). The Deep Range Imaging-OCT is a SS-OCT device that uses a wavelength-sweeping laser with a center wavelength of 1050 nm and a tuning range of approximately 100 nm. 100,000 A-scans are acquired per second with an 8-μm axial resolution in tissue.[18] For the present study, all eyes were imaged using two

Deep Range Imaging-OCT scan modes, wide-angle scan and 3D horizontal (H) disc circle grid scan. The Deep Range Imaging-OCT wide-angle 12 × 9 mm used a faster scan setting with the scan centered on the posterior pole. It was therefore possible to obtain images of the macular and ONH region in a single scan. The 12 × 9 mm scan comprises 256 B-scans, each comprising 512 A-scans for a total of 131,072 axial scans/volume. The total acquisition time was 1.3 seconds per 12 × 9 mm scan.

Deep Range Imaging-OCT segmentation software (version 9.12) was used to identify the limits of the RNFL as the area expanding from internal limiting membrane to the inner boundary of retinal ganglion cell layer, and then the RNFL thickness was determined throughout the scan. Data was exported using the manufacturer's OCT-Batch (version 4.3.0.118) utility. The quality of each scan and accuracy of the segmentation algorithm was independently reviewed by masked reviewers (Z.Y. and C.Z.). Three eyes were excluded from subsequent analyses, as their image quality scores were less than 50. In addition, 41 eyes were excluded due to clipped, poorly focused images, and images with segmentation failure and motion artifacts. In wide-angle scan, the Deep Range Imaging-OCT software calculates the average RNFL for each 1 mm^2 grid square of the 12 × 9 mm scan and allows this data to be displayed and exported. Figure 1 is an example of the graphical output provided by the Deep Range Imaging-OCT, which shows the average RNFL thicknesses in all 108 of the 1 × 1 mm squares of the 12 × 9 mm scan (Figure 1. Top). For the purposes of this report, the mean RNFL thickness over the entire 12 × 9 mm scan was calculated for each eye (global RNFL thickness). The mean RNFL thickness in different regions of the 12 × 9 mm scans was also analyzed to determine if a particular quadrant(s) had better diagnostic ability. After a review of all Deep Range Imaging-OCT wide-angle images in this study, we found that the location of optic disc varied over an area consisting of the central 9-square area (Figure 1, Bottom, red). Thus we removed RNFL measurements from this area. In addition, areas at the four corners of the wide-angle scan (A1, A2, A11, A12, B1, B12, C1, C12, G1, G12, H1, H12, I1, I2, I11, and I12, figure 1, Bottom, gray) often fell outside the fundus area from which the image was taken, and thus RNFL measurements from these sixteen squares were removed as well. Results for left eyes were transposed to right eyes. For sectoral analysis, we performed an analysis by quadrants, which were defined as shown in Figure 1, Bottom. Average RNFL thickness at the periphery of 12 × 9 mm wide-angle scan (Figure 1, Bottom, A3 – A10, D1, E1, F1, and I3 – I10) was also analyzed.

To measure peripapillary RNFL thickness, the Deep Range Imaging-OCT 3D (H) disc circle grid scan utilized the same 131,072 axial scans (512 A-scans for each of 256 B-scan) to acquire images from an area of 6 × 6 mm that is focused on the optic disc. Peripapillary RNFL thickness was then measured by automated placement of a circle of 3.4-mm in diameter, centered on the disc. Manual adjustment of circle placement was performed if necessary. This is equivalent to sampling 1024 A-scans along the circle. Average thicknesses of global peripapillary RNFL and superior, inferior, nasal and temporal quadrants were determined with the same segmentation software (version 9.12).

The Spectralis SD-OCT (software version 5.3.0.7, Heidelberg Engineering, Heidelberg, Germany) RNFL circle scan was also obtained. It consisted of 1536 A-scans with RNFL thickness measurements obtained on a 3.4mm diameter circle centered on the optic disc.

Global and sectoral peripapillary RNFL thickness measurements were calculated. All Spectralis images were reviewed by the UCSD Imaging Data Evaluation and Analysis Center to ensure the scan was centered, that the signal strength was > 15dB and that there were no artifacts. Scans that were inverted, clipped or those that had coexistent retinal pathological abnormalities were excluded. The RNFL segmentation algorithm was also manually adjusted to correct for segmentation errors.

Statistical Analysis

Normality assumption was assessed by inspection of histograms and using Shapiro-Wilk tests. Student *t*-tests were used for group comparison for normally distributed variables and Wilcoxon tests for non-normally distributed variables. Receiver operating characteristic (ROC) curves were constructed to assess the ability of each parameter to distinguish subjects with glaucoma from healthy controls. A ROC curve is a plot of the true-positive rate (TPR) versus the false-positive rate (FPR) for all possible cut-points. The area under the ROC curve was used to summarize the diagnostic accuracy of each parameter. An area under the ROC of 1.0 represents perfect discrimination, whereas an area of 0.5 represents chance discrimination.[19, 20] ROC curves were adjusted for age differences between healthy and glaucomatous eyes using an ROC regression model. This method has been described in detail previously.[21, 22] In the following linear regression model, $ROCx,x_D\ (q)$ is the sensitivity at the specificity of 1 – q. X represents the common covariates for healthy and glaucomatous eyes, such as age, and X_D represents disease-specific covariates such as disease severity. Φ is the normal cumulative distribution function. Coefficients α1 and α2 are the intercept and slope of the ROC curve.

$$ROCx,x_D\ (q) = \Phi\ (\alpha_1 + \alpha_2{}^{\Phi^{-1}}\ (q) + \beta X + \beta_D X_D)$$

Confidence intervals were obtained using a bootstrap resampling procedure (*n* = 1000 resamples). Observations from two eyes of the same subject are likely to be correlated, which can lead to underestimation of true variance. A between-cluster variance estimator was therefore used to account for correlations between eyes of the same subject and calculate robust variance estimates. All statistical analyses were performed with commercially available software (Stata version 13; StataCorp, College Station, TX).

RESULTS

One hundred and forty four glaucomatous eyes from 106 patients and sixty-six eyes from 42 healthy subjects were included. The demographic and clinical characteristics of healthy subjects and those with glaucoma are summarized in Table 1. Subjects with glaucoma were significantly older than healthy subjects with a mean (± standard deviation) age of 71.4 ± 10.2 years and 60.1 ± 12.8 years, respectively (P < 0.001). The average MD among glaucomatous eyes was −5.9 ± 6.4 dB, versus 0.2 ± 1.3 dB in healthy eyes. According to glaucoma severity,[23] 99 eyes had mild glaucoma (MD ≥ −6dB), 23 had moderate glaucoma (MD < −6 dB & ≥ −12dB), and 22 had severe glaucoma (MD < −12dB).

The global and sectoral measurements of RNFL thickness are summarized in Table 2. The mean (± standard deviation) wide-angle RNFL thickness using the 12×9 mm SS-OCT scan was 35.0 ± 9.6 μm in glaucomatous eyes compared to 50.5 ± 5.8 μm in healthy eyes (P <

0.001) (Figure 2). At the periphery of the 12 X 9 mm wide-angle scan (Figure 1, Bottom, A3 - A10, D1, E1, F1 and I3 - I10), average RNFL thickness was 30.3 ± 9.9 μm and 46.3 ± 6.2 μm in glaucomatous and healthy eyes, respectively (Table 2, $P < 0.001$). The mean peripapillary RNFL thickness measured with the 3D disc grid scan in SS-OCT was 72.9 ± 16.5 μm in glaucomatous eyes and 103.5 ± 12.3 μm in healthy eyes ($P < 0.001$). As a comparison, mean peripapillary RNFL thickness measured by SD-OCT was 70.2 ± 15.3 μm and 96.9 ± 9.0 μm for glaucomatous and healthy eyes, respectively. For both SS-OCT and SD-OCT, glaucomatous eyes also had significantly thinner RNFL than healthy eyes in all quadrants, including superior, inferior, nasal and temporal ($P < 0.001$ for all comparisons) (Table 2).

The area under the ROC curve was calculated for each parameter (Table 2 and Figure 3). The average RNFL thickness over the wide-angle SS-OCT scan had a performance similar to that of the SS-OCT average peripapillary RNFL thickness (0.88 ± 0.04 vs. 0.89 ± 0.04, respectively; $P = 0.556$). It also performed similarly to the SD-OCT average RNFL thickness on the circle scan (0.90 ± 0.04; $P = 0.342$) (Figure 3). At specificities of 80% and 95%, wide-angle RNFL thickness measured by SS-OCT had sensitivities of 77.0% and 44.3%, respectively. At corresponding specificities, the SS-OCT peripapillary RNFL thickness parameter had sensitivities of 80.3% and 41.0%, respectively. For the SD-OCT RNFL thickness parameter, the sensitivities at corresponding specificities were 82.0% and 45.9%, respectively.

For the SS-OCT wide-angle, the inferior quadrant had the best diagnostic accuracy (area under the ROC curve = 0.88) followed by the superior (0.83), temporal (0.81) and nasal quadrants (0.63). With the SS-OCT disc circle grid scan, the pattern was very similar. The inferior quadrant performed best (area under the ROC curve = 0.90), followed by the superior (0.83), temporal (0.73) and nasal quadrant (0.66). Results were slightly different with SD-OCT, in which the superior quadrant actually had the best diagnostic accuracy (0.93), followed by the inferior (0.88), nasal (0.71) and temporal quadrants (0.69).

Figure 4 shows an example of a glaucomatous eye. The wide-angle scan identified wedge-shaped loss of RNFL in the inferior quadrant, extending into the periphery of the 12×9 mm scan. In this eye there was clear correlation between the location of the RNFL defect present on SS-OCT, thinning of peripapillary RNFL detected by SD-OCT and damage seen on optic disc photographs and SAP.

DISCUSSION

In the present study, we assessed the ability of SS-OCT RNFL measurements to differentiate glaucomatous from healthy eyes. To our knowledge this is the first report to evaluate the ability of the SS-OCT wide-angle and peripapillary disc scan to detect glaucomatous damage. Our results indicated that the diagnostic accuracy of both the wide-angle and peripapillary RNFL thickness measured with SS-OCT were similar to that of peripapillary RNFL thickness measurements obtained with SD-OCT.

Average global RNFL thickness measurements acquired by the SS-OCT wide-angle scans were thinner than those obtained by the peripapillary RNFL scan, for both healthy and glaucomatous eyes. This is an expected result as the peripapillary region contains all the axons converging from the different locations in the retina, whereas measurements with the wide-angle scan protocol include areas located further away from the peripapillary region, containing only the axons that pass through the imaged area. Although peripheral RNFL thickness in 12 X 9 mm wide-angle scan was considerably thinner than peripapillary RNFL, it is still considerably thicker than the 8-μm axial resolution of this particular model of SS-OCT. Therefore, we expect that these RNFL thickness measurements would be reliable. However, future studies should evaluate the ability of measurements obtained with the wide-angle scan protocol to detect change over time.

Although the diagnostic ability of average RNFL measurements was similar with the wide-angle compared to the disc circle grid scans, the wide-angle scan may offer some advantages. For example, the extraction of RNFL data from the peripapillary circle scan may be limited by the need for an accurate placement of the scan around the optic disc by an operator. In contrast, placement of a peripapillary circle is not required with the wide-angle scan. In eyes with an atypical optic disc configuration, such as in those with tilted optic discs or extensive areas of peripapillary atrophy, placement of the peripapillary circle can be challenging due to difficulties in delineating the optic disc margins. Another advantage of the wide-angle scan is that it will potentially be less susceptible to artifacts that may affect the peripapillary circle measurements, such as those produced by floaters, localized scars, or extensive peripapillary atrophy extending to the region of the circle.

The wide-angle scan also allows information regarding the macula and optic disc to be captured in a single scan. This is of particular value given the growing realization of the importance of the macula for glaucoma monitoring.[24] The SS-OCT segmentation software allows segmentation of the retinal ganglion cell and inner plexiform layer thicknesses across the entire 12×9 mm scan. It may therefore provide a means for direct single-scan structure-structure comparisons of peripapillary and macular retinal layers. Further potential advantages of SS-OCT are that the longer wavelength light source is invisible, so that eye blinking during image acquisition may be reduced. Longer wavelength light may also result in less cataract-induced light scatter.

In addition to evaluating the diagnostic performance of RNFL thickness measured by the SS-OCT 12 X 9 mm wide-angle scan, we also determined the ability of peripapillary RNFL thickness, measured with SS-OCT 3D grid scan, in differentiating glaucomatous from healthy eyes. Peripapillary RNFL thickness measurements with SSOCT were slightly higher than those obtained with SD-OCT. It is unclear what might contribute to this small discrepancy between SS-OCT and SD-OCT. The numbers of axial scans sampled along the 3.4-mm measurement circle are 1024 in SS-OCT and 1536 in SD-OCT. However, despite the difference in the density of peripapillary RNFL sampling, no significant differences were found in the diagnostic accuracies of the different parameters.

In our study, we evaluated diagnostic accuracy by comparing measurements obtained in a group of patients with well-defined glaucomatous damage to those of healthy subjects.

Although our results may be seen as providing initial validation of SS-OCT measurements for detection of glaucomatous RNFL damage, it is important to emphasize that, in clinical practice, ancillary diagnostic tests are used to assist diagnosis in patients suspected of having the disease and not in those with clearly defined diagnoses.[25] Therefore, future studies should evaluate the diagnostic accuracy of SS-OCT in more challenging scenarios, such as detecting early damage in subjects suspected of having glaucoma.

The present study has limitations. The SS-OCT wide-scan protocol used in this study does not automatically exclude RNFL measurements in the region of the optic disc. In order to exclude these measurements, we evaluated which squares contained the location of the optic disc in the imaged subjects. The nine squares most frequently affected were then removed from further analysis. However, it is possible that the performance of SS-OCT wide-scan RNFL measurements could be improved by employing automated algorithms to exclude only the specific areas containing the optic disc for an individual eye. Another limitation of our study was that RNFL thickness from the nasal retina was only calculated from three squares as opposed to twenty-four squares for the temporal retina. This may have contributed to a lower performance of the nasal area as compared to the other sectors. However, previous studies have also not found a strong performance of the nasal area for glaucoma diagnosis using RNFL imaging.[26–29] Squares at the four corners often fell outside the scanned fundus area and, therefore, measurements from these squares were excluded from further analysis. However, no significant differences were found in diagnostic accuracy when the squares at the four corners of the 12 X 9 mm wide-scan were included in the analyses.

In conclusion, our results suggest that wide-angle and peripapillary RNFL measurements obtained using SS-OCT perform well in detecting glaucomatous damage to the RNFL. The improved scanning speed of SS-OCT allows acquisition of a more densely sampled wider posterior pole image than what is currently available with SD-OCT, however, the value of imaging an enlarged area remains to be determined.

ACKNOWLEDGEMENT

Funding/Support: Supported in part by National Institutes of Health/National Eye Institute grants EY021818 (F.A.M.), EY11008 (L.M.Z.), EY14267 (L.M.Z.), EY019869 (L.M.Z.), core grant P30EY022589, National Institutes of Health at Bethesda, Maryland; grants for participants' glaucoma medications from Alcon (Forth Worth, Texas), Allergan (Irvine, California), Pfizer (New York, New York), Merck (Whitehouse Station, New Jersey) and Santen (Osaka, Japan). Natural Science Foundation of Heilongjiang Province for Returned Scholars (Beijing China). No.LC2012C21 (C.Z.); Innovation research special fund of the Science and Technology of Heilong Jiang Province (Harbin, China), No.2011RFLYS029 (C.Z.). Scientific and technical research fund of Education Bureau of Heilongjiang Province (Harbin, China), No.12511311 (C.Z.); and an unrestricted grant from Research to Prevent Blindness (New York, New York).

REFERENCES

1. Harwerth RS, Carter-Dawson L, Smith EL, et al. Neural losses correlated with visual losses in clinical perimetry. Invest Ophthalmol Vis Sci. 2004; 45(9):3152–3160. [PubMed: 15326134]
2. Kass MA, Heuer DK, Higginbotham EJ, et al. The Ocular Hypertension Treatment Study: a randomized trial determines that topical ocular hypotensive medication delays or prevents the onset of primary open-angle glaucoma. Arch Ophthalmol. 2002; 120(6):701–713. discussion 829-730. [PubMed: 12049574]

3. Wollstein G, Schuman JS, Price LL, et al. Optical coherence tomography longitudinal evaluation of retinal nerve fiber layer thickness in glaucoma. Arch Ophthalmol. 2005; 123(4):464–470. [PubMed: 15824218]
4. Strouthidis NG, Scott A, Peter NM, Garway-Heath DF. Optic disc and visual field progression in ocular hypertensive subjects: detection rates, specificity, and agreement. Invest Ophthalmol Vis Sci. 2006; 47(7):2904–2910. [PubMed: 16799032]
5. Grewal DS, Tanna AP. Diagnosis of glaucoma and detection of glaucoma progression using spectral domain optical coherence tomography. Curr Opin Ophthalmol. 2013; 24(2):150–161. [PubMed: 23328662]
6. Leung CK, Cheung CY, Weinreb RN, et al. Evaluation of retinal nerve fiber layer progression in glaucoma: a study on optical coherence tomography guided progression analysis. Invest Ophthalmol Vis Sci. 2010; 51(1):217–222. [PubMed: 19684001]
7. Medeiros FA, Alencar LM, Zangwill LM, Sample PA, Weinreb RN. The Relationship between intraocular pressure and progressive retinal nerve fiber layer loss in glaucoma. Ophthalmology. 2009; 116(6):1125–1133. [PubMed: 19376584]
8. Chinn SR, Swanson EA, Fujimoto JG. Optical coherence tomography using a frequency-tunable optical source. Opt Lett. 1997; 22(5):340–342. [PubMed: 18183195]
9. Mansouri K, Medeiros FA, Marchase N, et al. Assessment of choroidal thickness and volume during the water drinking test by swept-source optical coherence tomography. Ophthalmology. 2013; 120(12):2508–2516. [PubMed: 24021895]
10. Mrejen S, Spaide RF. Optical coherence tomography: imaging of the choroid and beyond. Surv Ophthalmol. 2013; 58(5):387–429. [PubMed: 23916620]
11. Mansouri K, Nuyen B, R NW. Improved visualization of deep ocular structures in glaucoma using high penetration optical coherence tomography. Expert Rev Med Devices. 2013; 10(5):621–628. [PubMed: 23972075]
12. Takayama K, Hangai M, Kimura Y, et al. Three-dimensional imaging of lamina cribrosa defects in glaucoma using swept-source optical coherence tomography. Invest Ophthalmol Vis Sci. 2013; 54(7):4798–4807. [PubMed: 23778878]
13. Park HY, Shin HY, Park CK. Imaging the posterior segment of the eye using swept-source optical coherence tomography in myopic glaucoma eyes: comparison with enhanced-depth imaging. Am J Ophthalmol. 2014; 157(3):550–557. [PubMed: 24239773]
14. Sample PA, Girkin CA, Zangwill LM, et al. The African Descent and Glaucoma Evaluation Study (ADAGES): design and baseline data. Arch Ophthalmol. 2009; 127(9):1136–1145. [PubMed: 19752422]
15. Racette L, Chiou CY, Hao J, et al. Combining functional and structural tests improves the diagnostic accuracy of relevance vector machine classifiers. J Glaucoma. 2010; 19(3):167–175. [PubMed: 19528827]
16. Medeiros FA, Vizzeri G, Zangwill LM, et al. Comparison of retinal nerve fiber layer and optic disc imaging for diagnosing glaucoma in patients suspected of having the disease. Ophthalmology. 2008; 115(8):1340–1346. [PubMed: 18207246]
17. Medeiros FA, Weinreb RN, Sample PA, et al. Validation of a predictive model to estimate the risk of conversion from ocular hypertension to glaucoma. Arch Ophthalmol. 2005; 123(10):1351–1360. [PubMed: 16219726]
18. Mansouri K, Medeiros FA, Tatham AJ, Marchase N, Weinreb RN. Evaluation of retinal and choroidal thickness by swept-source optical coherence tomography: repeatability and assessment of artifacts. Am J Ophthalmol. 2014; 157(5):1022–1032. [PubMed: 24531020]
19. Obuchowski NA. ROC analysis. AJR Am J Roentgenol. 2005; 184(2):364–372. [PubMed: 15671347]
20. DeLong ER, DeLong DM, Clarke-Pearson DL. Comparing the areas under two or more correlated receiver operating characteristic curves: a nonparametric approach. Biometrics. 1988; 44(3):837–845. [PubMed: 3203132]
21. Dodd LE, Pepe MS. Partial AUC estimation and regression. Biometrics. 2003; 59(3):614–623. [PubMed: 14601762]

22. Medeiros FA, Sample PA, Zangwill LM, et al. A statistical approach to the evaluation of covariate effects on the receiver operating characteristic curves of diagnostic tests in glaucoma. Invest Ophthalmol Vis Sci. 2006; 47(6):2520–2527. [PubMed: 16723465]

23. Brusini P, Johnson CA. Staging functional damage in glaucoma: review of different classification methods. Surv Ophthalmol. 2007; 52(2):156–179. [PubMed: 17355855]

24. Hood DC, Raza AS, de Moraes CG, Liebmann JM, Ritch R. Glaucomatous damage of the macula. Prog Retin Eye Res. 2013; 32:1–21. [PubMed: 22995953]

25. Medeiros FA. How should diagnostic tests be evaluated in glaucoma? Br J Ophthalmol. 2007; 91(3):273–274. [PubMed: 17322462]

26. Leite MT, Rao HL, Zangwill LM, Weinreb RN, Medeiros FA. Comparison of the diagnostic accuracies of the Spectralis, Cirrus, and RTVue optical coherence tomography devices in glaucoma. Ophthalmology. 2011; 118(7):1334–1339. [PubMed: 21377735]

27. Leung CK, Lam S, Weinreb RN, et al. Retinal nerve fiber layer imaging with spectral-domain optical coherence tomography: analysis of the retinal nerve fiber layer map for glaucoma detection. Ophthalmology. 2010; 117(9):1684–1691. [PubMed: 20663563]

28. Akashi A, Kanamori A, Nakamura M, et al. Comparative assessment for the ability of Cirrus, RTVue, and 3D-OCT to diagnose glaucoma. Invest Ophthalmol Vis Sci. 2013; 54(7):4478–4484. [PubMed: 23737470]

29. Rao HL, Zangwill LM, Weinreb RN, et al. Comparison of different spectral domain optical coherence tomography scanning areas for glaucoma diagnosis. Ophthalmology. 2010; 117(9): 1692–1699. [PubMed: 20493529]

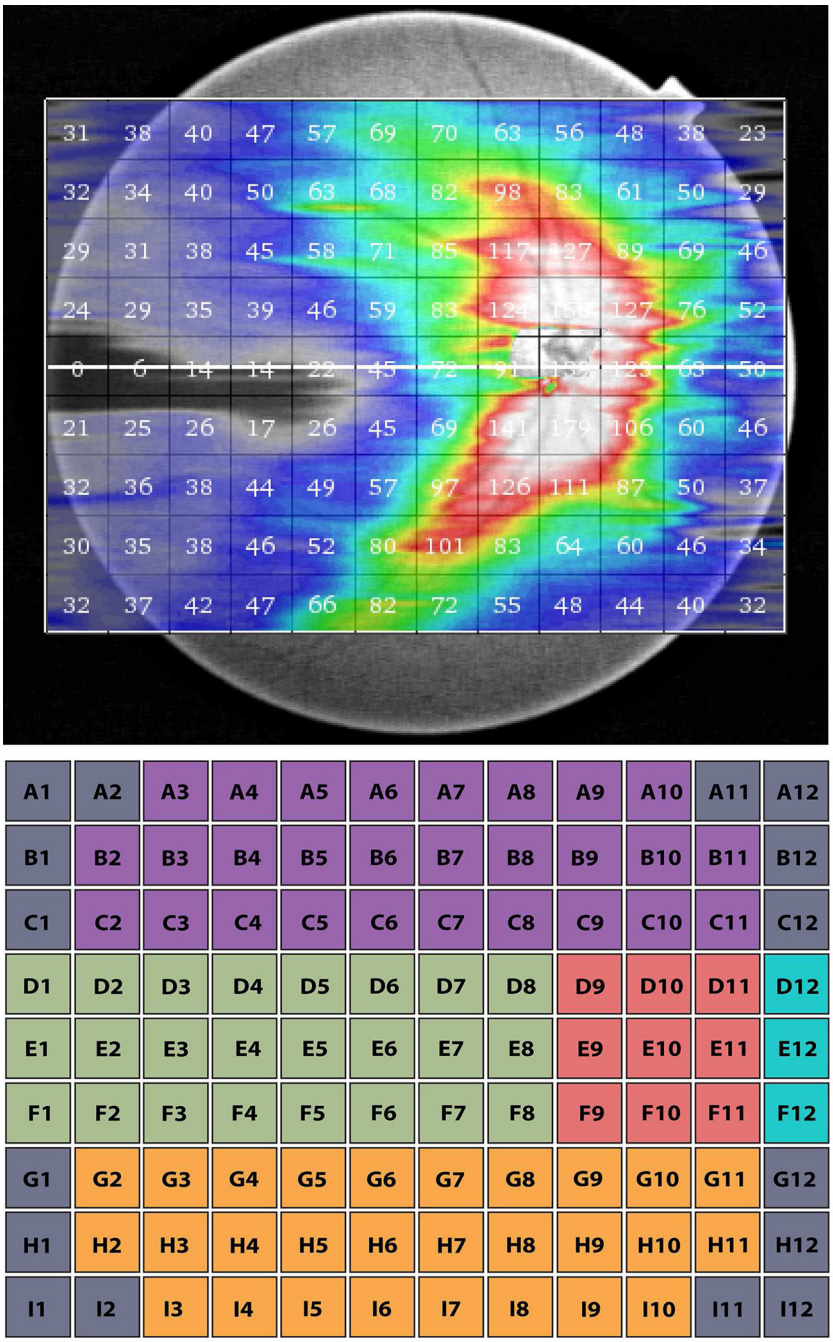

Figure 1.

Swept source optical coherence tomography wide-angle scan. Top: Swept source optical coherence tomography (SS-OCT) 12×9 mm wide-angle retinal nerve fiber layer thickness map (right eye) showing measurements in each of the 108 1×1 mm squares. Bottom: representation of the retinal areas as determined for the right eye, with nasal quadrant (cyan), temporal quadrant (green), superior quadrant (purple), inferior quadrant (orange), and optic disc (red). Squares at the four corners (gray) were excluded from the calculations.

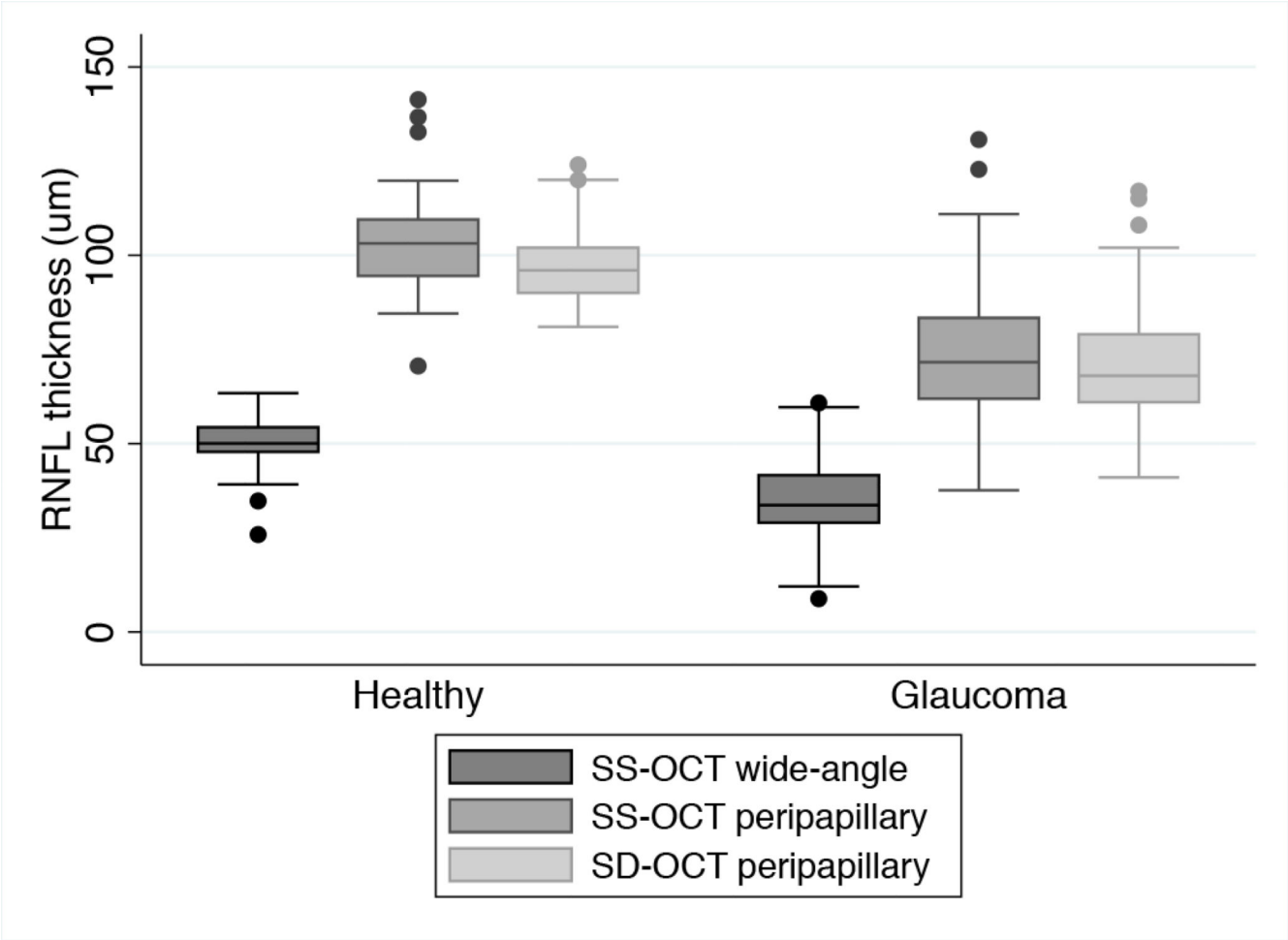

Figure 2.
Box plots illustrating the distribution of retinal nerve fiber layer thickness measurements with the different scan protocols in glaucomatous and healthy eyes.

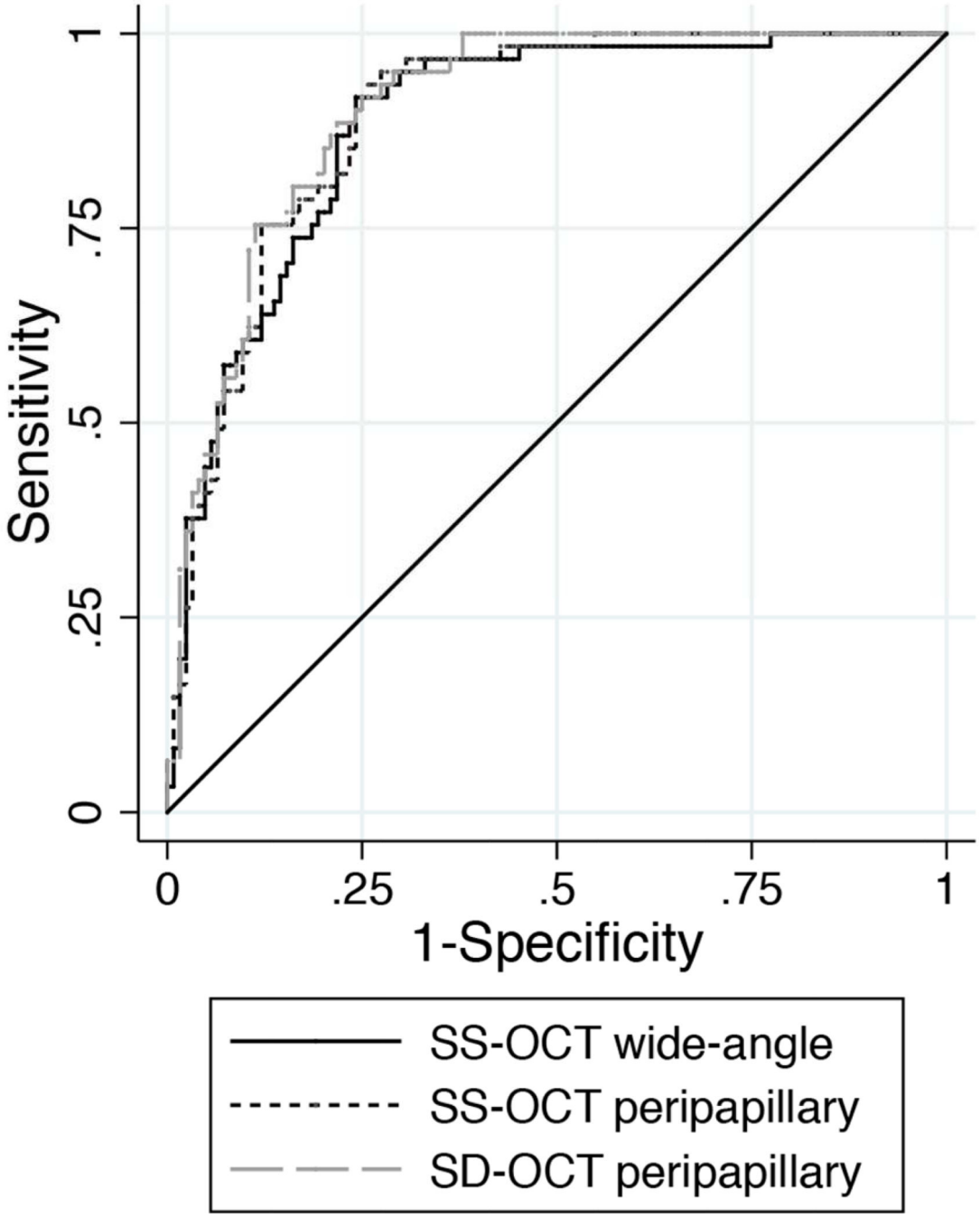

Figure 3.
Receiver operating characteristic curves to discriminate glaucomatous from healthy eyes for the different scan protocols used in the study.

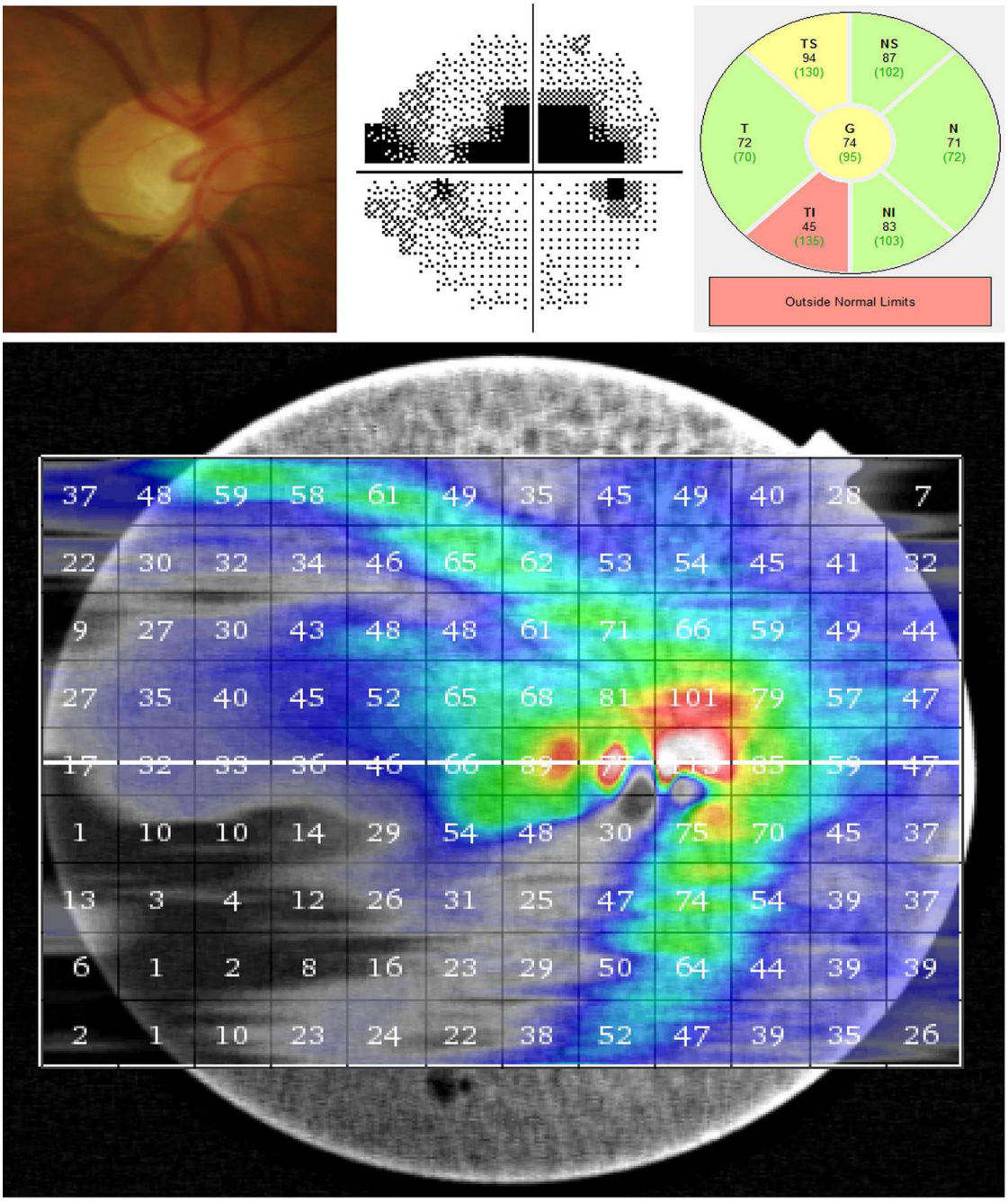

Figure 4.

Example of retinal nerve fiber layer thinning in a glaucomatous eye detected by the swept source optical coherence tomography wide-angle scan. Top left, Optic disc photograph showing inferotemporal neuroretinal rim thinning. Top middle, Standard automated perimetry showing a corresponding superior visual field defect. Top right, Spectral domain optical coherence tomography scan showing retinal nerve fiber layer thinning in the

inferotemporal peripapillary sector. Bottom, swept source optical coherence tomography wide-angle scan showing an inferotemporal wedge-shaped defect in the nerve fiber layer.

Table 1

Demographic and clinical characteristics of glaucoma patients and healthy subjects who were imaged with swept source optical coherence tomography and spectral domain optical coherence tomography in the study.

	Healthy (66 eyes, 42 subjects)	Glaucoma (144 eyes, 106 subjects)	P value
Gender, Female (n)	27 (64.3%)	50 (47.2%)	0.085[a]
Age (years)	60.1 ±12.8	71.4± 10.2	<0.001[b]
Ancestry			
African (n)	16(38.1%)	27 (25.5%)	0.161 [a]
European (n)	23 (54.8%)	68 (64.2%)	
Other (n)	3(7.1%)	11 (10.4%)	
Visual field mean deviation (dB)	0.2 ±1.3	−5.9 ±6.4	<0.001 [b]
Intraocular pressure (mmHg)	13.4 ±2.5	14.1 ±4.1	0.125[b]

Values correspond to mean ± standard deviation unless noted otherwise.

[a] Chi square test,

[b] Two-sample t test

Table 2

Retinal nerve fiber layer thickness and areas under the receiver operating characteristic curves for swept source optical coherence tomography and spectral domain optical coherence tomography parameters.

RNFL thicknesses (μm) (mean ± SD)	Glaucoma	Healthy	*P* Value	Area under the ROC curve (SE)
Global RNFL				
SS-OCT wide-angle	35.0 ±9.6	50.5 ±5.8	<0.001	0.88 (0.04)
SS-OCT peripapillary	72.9 ±16.5	103.5 ±12.3	<0.001	0.89 (0.04)
SD-OCT peripapillary	70.2 ±15.3	96.9 ±9.0	<0.001	0.90 (0.04)
Sectoral RNFL				
SS-OCT (wide-anqle)				
Periphery	30.3 ±9.9	46.3 ±6.2	<0.001	0.90 (0.04)
Nasal quadrant	33.1 ±14.9	45.1 ±10.8	<0.001	0.63 (0.06)
Temporal quadrant	25.4 ±7.1	31.9±3.9	<0.001	0.81 (0.05)
Superior quadrant	41.1 ±12.3	59.0 ±7.9	<0.001	0.83 (0.05)
Inferior quadrant	36.4 ±14.0	57.2 ±7.3	<0.001	0.88 (0.04)
SS-OCT (disc scan)				
Nasal peripapillary	68.0 ±22.8	87.2 ±23.6	<0.001	0.66 (0.06)
Temporal peripapillary	57.1 ±14.5	71.3± 12.6	<0.001	0.73 (0.06)
Superior peripapillary	79.2 ±22.9	112.5 ±18.2	<0.001	0.83 (0.05)
Inferior peripapillary	87.5 ±30.4	142.7 ±24.6	<0.001	0.90 (0.04)
SD-OCT (circle scan)				
Nasal peripapillary	58.0 ±16.2	73.8 ±13.5	<0.001	0.71 (0.07)
Temporal peripapillary	57.7 ±15.5	68.0 ±12.4	<0.001	0.69 (0.06)
Superior peripapillary	83.1 ±20.4	121.8 ±13.6	<0.001	0.93 (0.03)
Inferior peripapillary	84.2 ±27.4	126.0 ±13.2	<0.001	0.88 (0.05)

* Area under the receiver operating characteristic (ROC) curve was adjusted for differences in age between healthy and glaucomatous subjects.
RNFL= retinal nerve fiber layer; SD = standard deviation; SE = standard error; SS-OCT = swept source optic coherence tomography; SD-OCT = spectral domain optic coherence tomography.